
Parameter-Efficient Electromagnetic Surrogate Solver for Broadband Field Prediction using Discrete Wavelength Data

Joonhyuk Seo ^{*1} Chanik Kang ^{*1} Dongjin Seo ² Haejun Chung ¹

Abstract

Recently, electromagnetic surrogate solvers, trained on solutions of Maxwell’s equations under specific simulation conditions, enabled real-time inference of computationally expensive simulations. However, conventional surrogate solvers often consider only a narrow range of simulation parameters and fail when encountering even slight variations in simulation conditions. To address this limitation, we propose a broadband surrogate solver capable of providing solutions across a continuous range of wavelengths, even when trained on discrete wavelength data. Our approach leverages a Wave-Informed element-wise Multiplicative Encoding and a Fourier Group Convolutional Shuffling operator to mitigate overfitting while capturing the fundamental characteristics of Maxwell’s equations. Compared to the state-of-the-art surrogate solver, our model achieves a 74% reduction in parameters, an 80.5% improvement in prediction accuracy for untrained wavelengths, demonstrating superior generalization and efficiency.

1. Introduction

The development of deep learning models for predicting solutions to partial differential equations (PDEs) has garnered significant attention in recent years. In particular, deep learning applications in fluid dynamics (Brunton et al., 2020), thermodynamics (Zhou & Huang, 2024), and electromagnetics (Kuznetsov et al., 2024) have been of great interest. In electromagnetics, where Maxwell’s equations are the governing physics, the design and optimization of meta-optical devices present substantial computational challenges due to their large-scale dimensions, often exceeding 100,000 wavelengths (Li et al., 2022c; Xue et al., 2023; Kang et al., 2024a). Consequently, the development of ultra-fast surrogate solvers for predicting solutions to Maxwell’s equations has the potential to revolutionize simulation processes in this field.

Among the various important applications of electromagnet-

ics, including metalenses (Setareh et al., 2024; Lee et al., 2024; Seo et al., 2023; Chung & Miller, 2020), waveguides for integrated quantum and photonic circuits (Wang et al., 2020), mode converters (Bae et al., 2024), and photonic crystals (Yoon et al., 2016; Gold et al., 2024), we focus on metalens simulations as the primary subject of our research. This choice is motivated by the significant computational challenges associated with their large simulation domains.

Conventional surrogate solvers often utilize neural operators (Kovachki et al., 2023; Li et al., 2020; Tran et al., 2021; Li et al., 2023; Raonic et al., 2023; Rahman et al., 2022; Li et al., 2024a; Hao et al., 2023; Li et al., 2022a), which exhibit discretization invariance while effectively learning the underlying characteristics of PDEs. Among these, the Fourier Neural Operator (FNO) has shown promising inference capabilities across various electromagnetic applications (Li et al., 2022b; Pathak et al., 2022; Kang et al., 2024b), making it a strong candidate for accelerating computationally expensive simulations. However, FNO often fails to predict a solution of the PDEs for different simulation environments such as changes in wavelength, source configuration, or boundary conditions. To address this limitation, effective conditioning mechanisms, such as incorporating additional vectors or modulated weights within the Fourier layers, are required to enhance the adaptability and generalization of the model. However, state-of-the-art EM surrogate solvers still struggle to provide an accurate inference to unseen simulation environments, emphasizing the need for further development in this area.

Moreover, FNO encounters a significant challenge related to parameter complexity. In particular, for a 2D problem, each layer in FNO requires $C^2 M_v M_h$, where M_v and M_h denote the number of frequency modes in the vertical and horizontal directions, respectively, and C represents the number of channels. As a result, FNO can become excessively large, leading to a heavily parameterized network with increased computational demands and slow inference speed.

One of the most parameter-efficient approaches for learning EM simulations is *NeurOLight* (Gu et al., 2022), which addresses both the parameter complexity and the conditioning challenges faced by surrogate solvers. Furthermore, *NeurOLight* demonstrates the generalization capability of

limitedly observed wavelengths by assessing the prediction performance for unseen wavelengths during training. Despite these strengths, NeurOLight’s reliance on minor grid step variations and conditioning through simple concatenation with input data restricts its learning and inference capabilities to a limited range of wavelengths and grid steps.

In this work, we significantly enhance the capability of our FNO-based EM surrogate solver to generalize to unseen simulation environments while simultaneously improving parameter efficiency. To achieve this, we introduce two key ideas: (i) Wave-Informed element-wise Multiplicative Encoding (WIME) and (ii) Fourier Group Convolutional Shuffling (FGCS) operator. By incorporating these techniques, the proposed model demonstrates highly accurate inference of EM solutions across a continuous and broad range of wavelengths, even when trained on relatively wide-spaced discrete wavelength data.

2. Background and Motivation

2.1. Fundamentals of the Electromagnetic Simulations

Light can be treated as an electromagnetic wave, and its propagation is governed by Maxwell’s equations, a set of coupled PDEs describing how electric and magnetic fields evolve in space and time. Under time-harmonic conditions (with $e^{-j\omega t}$ dependence), Maxwell’s equations simplify to the frequency-domain form:

$$\nabla \times \mathbf{E}(\mathbf{r}) = -j\omega\mu_0\mathbf{H}(\mathbf{r}), \tag{1}$$

$$\nabla \times \mathbf{H}(\mathbf{r}) = j\omega\epsilon_0\epsilon_r(\mathbf{r})\mathbf{E}(\mathbf{r}), \tag{2}$$

where $\mathbf{E}(\mathbf{r})$ and $\mathbf{H}(\mathbf{r})$ are the electric and magnetic fields, respectively. Here, ω is the angular frequency, μ_0 and ϵ_0 are the permeability and permittivity of free space, and $\epsilon_r(\mathbf{r})$ is the relative permittivity distribution in the medium.

By substituting (1) into (2), we eliminate one of the fields and arrive at a vector Helmholtz-type PDE in terms of $\mathbf{E}(\mathbf{r})$:

$$\nabla \times \nabla \times \mathbf{E}(\mathbf{r}) - k_0^2\epsilon_r(\mathbf{r})\mathbf{E}(\mathbf{r}) = 0, \tag{3}$$

where $k_0 = \omega\sqrt{\mu_0\epsilon_0}$ is the free-space wavenumber. This Helmholtz equation, governing the spatial distribution of the electric field, represents the PDE we seek to approximate using a surrogate solver.

To generate the training and validation datasets necessary for building our surrogate solver, we use the Finite-Difference Frequency-Domain (FDFD) method (Hughes et al., 2019; 2018). FDFD discretizes the spatial domain into a grid and applies finite differences to approximate spatial derivatives, enabling the efficient computation of steady-state electromagnetic fields for a given frequency. This approach is particularly well-suited for analyzing metalens structures, where complex subwavelength features can give rise to strong resonance effects, as illustrated in Fig 5.

Such resonances often exhibit highly nonlinear responses to changes in wavelength, making it difficult for a surrogate solver trained at a set of discrete wavelengths to predict fields at other wavelengths accurately. This wavelength-dependent nonlinearity poses a challenge for surrogate solvers.

2.2. Advancements in Operator Learning

The input and output of PDEs are defined as functions on bounded domains (Kovachki et al., 2023). Neural operators are well-suited to map between function spaces; thus, they have been widely studied. They satisfy discretization invariance, demonstrating robust results with varying mesh sizes. Recent advancements in the field of operator learning, including transformer-based neural operators (Cao, 2021; Hao et al., 2023; Li et al., 2022a; 2024b), convolution neural operators (Raonic et al., 2023), and Fourier neural operators (Azizzadenesheli et al., 2024; Li et al., 2020; Tran et al., 2021; Li et al., 2023; 2024a; Gu et al., 2022), offer promising solutions that effectively learn PDE characteristics while preserving discretization invariance.

Specifically, FNO (Li et al., 2020) presents a deep learning architecture to learn mappings between infinite-dimensional function spaces. This approach significantly improves performance and efficiency on a variety of challenging applications. After FNO has been published, the Factorized-FNO (Tran et al., 2021), named F-FNO, further improves the performance of the original FNO by using separable spectral layers and enhanced residual connections, significantly reducing errors in various PDE problems.

In the inference of electromagnetic simulation results, the state-of-the-art model NeurOLight (Gu et al., 2022) leverages the FNO. NeurOLight encodes joint PDE representation by incorporating wavelength and material permittivity with the given PDE. NeurOLight has demonstrated superior parameter efficiency and greater accuracy compared to previous studies. However, NeurOLight is limited in its ability to predict fields across a broad range of wavelengths and grid steps, restricting its applicability to broadband wavelength simulation. In this study, we focus on the generalization capability for limited conditions, specifically wavelengths, by proposing WIME conditioning that enables accurate prediction for intermediate wavelengths of trained wavelengths. Moreover, we further significantly improve the parameter efficiency by introducing the FGCS operator based on weight-grouping and weight-sharing schemes.

2.3. Motivation

The resonance effects in electromagnetic systems exhibit highly nonlinear and complex variations across continuously changing wavelengths. Consequently, predicting fields at unobserved intermediate wavelengths, which lie between

the discrete wavelengths seen during training, remains a significant challenge.

In most cases, the parameters of physical phenomena modeled by PDEs are inherently continuous. Therefore, accurately capturing these continuous parameters is necessary to construct a reliable surrogate solver for the underlying physical system. To achieve this, it is essential to ensure robust predictions not only for the parameter values observed during training but also for the parameter values unobserved during training.

Evaluating the model’s generalization capability for these unseen parameters allows us to assess its ability to capture the broad and continuous spectrum of physical systems. A surrogate solver capable of accurately predicting across this continuous parameter space can provide a trustworthy alternative to traditional numerical solvers.

Motivated by the above claims, we determined to focus on exploring the generalization capability regarding limitedly observed condition values during training.

3. Methodology

3.1. Problem Setting

Let $\Omega \subset \mathbb{R}^d$, $\mathcal{A} = \mathcal{A}(\Omega; \varepsilon^{d_a})$ where $\varepsilon = \{\varepsilon_{\text{air}}, \varepsilon_{\text{material}}\}$, and $\mathcal{U} = \mathcal{U}(\Omega; \mathbb{C}^{d_u})$ be a bounded open set of the underlying domain, infinite-dimensional spaces of the relative permittivity and electric field of the simulation. ε_{air} and $\varepsilon_{\text{material}}$ represent the relative permittivity values of air and material. Additionally, we assume that $\mathcal{W} \subset \mathbb{R}_{\geq 0}$ is the broadband range, such as the visible light spectrum, and $\tilde{\mathcal{W}} \subset \mathcal{W}$ is a discrete collection of wavelengths evenly distributed at a specific interval from \mathcal{W} . Our model \mathcal{G}_θ learns an ideal electromagnetic simulator $\mathcal{G}^\dagger : \mathcal{A} \rightarrow \mathcal{U}$ for continuous wavelengths \mathcal{W} by mapping between infinite-dimensional function spaces using a finite set of Maxwell PDE input-output pairs $\{(w_j, a_j), u_j\}_{j=1}^N$, where $w \in \tilde{\mathcal{W}}$.

3.2. Model Architecture

Similar to a prior work (Kovachki et al., 2023), our model has an iterative process to map between infinite-dimensional function spaces.

$$u = \mathcal{G}_\theta(a) = (\mathcal{Q} \circ \mathcal{L}^{(L)} \circ \dots \circ \mathcal{L}^{(1)} \circ \mathcal{P})(a) \quad (4)$$

where $\mathcal{L}^{(l)}$ is a l -th operator layer, L indicates the number of layers, and \mathcal{P}, \mathcal{Q} are lifting and projection operators, respectively.

We define the layers $\mathcal{L}^{(l)}$ as follows:

$$\mathcal{L}^{(l)}(z^{(l)}) = z^{(l)} + W_2^{(l)} \sigma(W_1^{(l)} \tilde{\mathcal{K}}^{(l)}(z^{(l)}) + b_1^{(l)}) + b_2^{(l)} \quad (5)$$

where $\tilde{\mathcal{K}}^{(l)}$ is our kernel integral operator based on the Fourier transform detailed in Section 3.2.1.

We employ a residual connection after two linear transformations with an activation function to enhance the capacity of our model, like (Vaswani et al., 2017; Tran et al., 2021). In addition, we use 1×1 convolution layers instead of 3×3 convolution layers to ensure discretization invariance, unlike a previous study (Gu et al., 2022).

3.2.1. KERNEL INTEGRAL OPERATOR $\tilde{\mathcal{K}}$

The kernel integral operator in the original FNO is defined as follows:

$$\mathcal{K}^{(l)} = \mathcal{F}^{-1}(R^{(l)} \cdot \mathcal{F}), \quad R \in \mathbb{C}^{M_v \times M_h \times C \times C} \quad (6)$$

where \mathcal{F} is a Fourier transformation, M_v, M_h , and C denote the number of frequency modes of vertical and horizontal components and the number of channels, respectively. Thus, the number of parameters in a 2D problem is $C^2 M_v M_h$. This results in a substantially high parameter complexity. Thus, as illustrated in Figure 1 (top), we construct the cross-shaped block (Gu et al., 2022) to achieve superior parameter efficiency. We split the inputs into two chunks $z^{(l)} = [z_h^{(l)}, z_v^{(l)}]$ along the channel axis and factorize the Fourier transforms over the horizontal and vertical dimensions $\tilde{\mathcal{K}}^{(l)}(z^{(l)}) = [\mathcal{K}_h^{(l)}(z_h^{(l)}), \mathcal{K}_v^{(l)}(z_v^{(l)})]$. Therefore, the weights $R_h^{(l)} \in \mathbb{C}^{M_h \times \frac{1}{2}C \times \frac{1}{2}C}$ and $R_v^{(l)} \in \mathbb{C}^{M_v \times \frac{1}{2}C \times \frac{1}{2}C}$ of both two blocks have $\frac{C^2}{4}(M_h + M_v)$ parameters, which is significantly fewer than the $C^2 M_h M_v$ parameters in the kernel integral operator of FNO.

Furthermore, we propose an efficient Fourier Group Convolution Shuffling (FGCS) operator, which achieves high parameter efficiency while maintaining strong performance, as illustrated in Figure 1 (top and bottom). Our approach applies grouping in the Fourier domain along the channel dimension, introducing the group parameter G in a weight-sharing manner, as inspired by (Xie et al., 2017; Guibas et al., 2021; Kim et al., 2024).

To provide a detailed discussion of the FGCS operator, we define the Fourier transformed input feature as $v^{(l)}$ in a l -th layer. For simplicity, we only consider vertical axis FGCS operation. Thus the feature’s shape would be $v^{(l)} \in \mathbb{C}^{M \times W \times \frac{1}{2}C}$.

First, we reshape the tensor $v^{(l)}$ (The symbol \Rightarrow denotes a tensor reshaping notation):

$$v^{(l)} \in \mathbb{C}^{M \times W \times \frac{1}{2}C} \Rightarrow v^{(l)} \in \mathbb{C}^{M \times W \times G \times \frac{1}{2G}C} \quad (7)$$

Then, we apply matrix multiplication with a shared weight matrix $R^{(l)} \in \mathbb{C}^{M \times \frac{C}{2G} \times \frac{C}{2G}}$ in the spectral domain:

$$v'_{i,j,p,q}{}^{(l)} = \sum_{k=1}^{\frac{1}{2G}C} v_{i,j,p,k}{}^{(l)} R_{i,k,q}{}^{(l)} \quad (8)$$

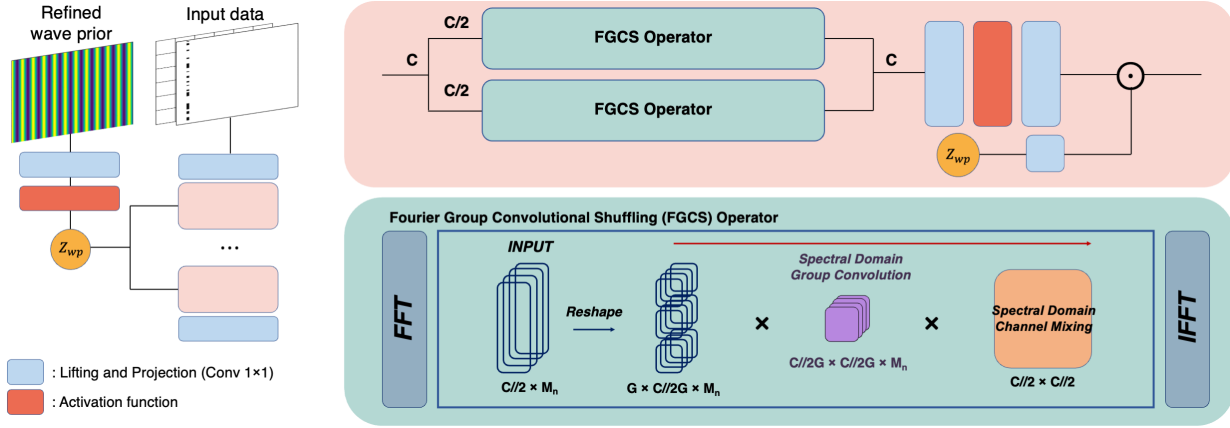


Figure 1: Schematic illustration of (left) the proposed overall framework including (top) each layer and Wave-Informed element-wise Multiplicative Encoding (WIME) and (bottom) Fourier Group Convolution Shuffling (FGCS) operator.

Subsequently, we conduct an additional tensor reshaping to make the shape of feature $v^{(l)}$ be the original tensor shape $M \times W \times \frac{1}{2}C$:

$$v^{(l)} \in \mathbb{C}^{M \times W \times G \times \frac{1}{2}C} \Rightarrow v^{(l)} \in \mathbb{C}^{M \times W \times \frac{1}{2}C} \quad (9)$$

However, the weight-sharing scheme in the group convolution introduces significant information loss, leading to a substantial decline in performance. To mitigate this issue, we implement channel shuffling in the Fourier domain, which can be efficiently performed through matrix multiplication along the channel dimension using $W_{\text{ch}}^{(l)} \in \mathbb{C}^{\frac{1}{2}C \times \frac{1}{2}C}$:

$$v_{i,j,p}^{(l)} = \sum_k^{\frac{C}{2}} v_{i,j,k}^{(l)} W_{\text{ch } k,p}^{(l)} \quad (10)$$

The channel shuffling scheme can compensate for the lost information by weight-sharing group convolution, thereby preserving performance while achieving exceptional parameter efficiency.

3.2.2. WAVE-INFORMED ELEMENT-WISE MULTIPLICATIVE ENCODING

The variations in electric field patterns with changing wavelengths, caused by resonance and diffraction phenomena during light-matter interactions, are highly complex. This complexity poses challenges in accurately predicting simulation fields for wavelengths unobserved during training. In this case, it is crucial to incorporate condition embeddings that accurately captures the wave characteristics and to adopt a conditioning method that properly integrates this information into the model.

We propose Wave-Informed element-wise Multiplicative Encoding (WIME) to enable generalized field prediction

at unseen wavelengths, as illustrated in Figure 1 (left and top). We assume that the condition embeddings have high similarity with the fields, effectively capturing the key characteristics of wave patterns. The condition embeddings are denoted as $\mathcal{W} \in \mathbb{R}^{H \times W \times 2}$. A detailed explanation of the condition embeddings will be provided in Section 3.2.3.

Based on these assumptions, preserving the spatial structure of the condition embeddings is essential to accurately capture the variations in field patterns across continuously changing wavelengths. To ensure this, we exclusively utilize channel-wise operations (1×1 convolutional layer) for processing the condition embeddings, thereby maintaining their spatial structure throughout the transformation.

First, we create a common embedding, which is then injected into all layers, using a 1×1 convolutional layer w^{wp} with a nonlinear activation function σ :

$$z_{i,j,p}^{wp} = \sigma\left(\sum_k^2 W_{i,j,k} w_{k,p}^{wp}\right) \quad (11)$$

Then, each layer adaptively transforms the embedding using an additional 1×1 convolutional layer $w^{(l)}$:

$$z_{i,j,p}^{wp,(l)} = \sum_k^C z_{i,j,k}^{wp} w_{k,p}^{(l)} \quad (12)$$

The final condition embeddings $z^{wp,(l)}$ created in each layer are element-wisely multiplied with the output of the feed-forward network $z^{(l)}$ before the residual connection in each layer:

$$\mathcal{L}^{(l)}(z^{(l)}) = z^{(l)} + z^{(l)} \odot z^{wp,(l)} \quad (13)$$

where $z^{(l)}$ refers to $W_2^{(l)} \sigma(W_1^{(l)} \tilde{\mathcal{K}}^{(l)}(z^{(l)} + b_1^{(l)}) + b_2^{(l)})$ in eq (5). By injecting the condition into all layers through element-wise multiplication, we strongly regularize the spatial and structural information of the field patterns according to the varying wavelengths while satisfying discretization invariance.

3.2.3. REFINED WAVE PRIOR

We construct condition embeddings that accurately capture wave characteristics by incorporating a wave prior (Gu et al., 2022). The wave prior $\mathcal{W} = [\mathcal{W}_x, \mathcal{W}_y]$ is an artificial wave pattern derived from the solution of the wave equation where \mathcal{W}_x and \mathcal{W}_y are expressed as $\mathcal{W}_x = e^{j\frac{2\pi\sqrt{\epsilon_r}}{\lambda}x} \mathbf{1}^T \Delta l_x$ and $\mathcal{W}_y = e^{j\frac{2\pi\sqrt{\epsilon_r}}{\lambda}y} \mathbf{1}^T \Delta l_y$. Here, $\epsilon_r \in \mathbb{C}^{H \times W}$ represents the relative permittivity of the structures at each coordinate, λ is the wavelength, Δl_x and Δl_y denote the simulation step sizes. The variables x and y correspond to the spatial coordinates. Since the wave prior is derived from the solution of the wave equation, it closely resembles the wave patterns of the fields generated by the simulator, which result from light propagation according to wavelength. This inherent similarity ensures that the constructed embeddings align well with the underlying assumptions of the model.

However, note that the wave prior considers only the permittivity values of the structures and does not account for diffraction phenomena, as it is defined by substituting coordinates without modeling wave interactions. Consequently, it exhibits sharp and physically implausible features in regions where the permittivity changes, particularly under specific simulation settings where electric fields are continuous at material boundaries. Moreover, WIME employs a shallow 1×1 convolutional layer to preserve the spatial structure of the condition embeddings. While this design choice helps maintain spatial structure, it also limits the ability to capture complex diffraction effects arising from light-structure interactions. As a result, physically implausible artifacts introduced by the wave prior can persist in the model’s output. We will present these artifacts in Section 4.3.2 and analyze their impact on the model’s performance.

Hence, we propose a refined wave prior that excludes the ϵ_r term, defined as $\mathcal{W}_x = e^{j\frac{2\pi}{\lambda}x} \mathbf{1}^T \Delta l_x$ and $\mathcal{W}_z = e^{j\frac{2\pi}{\lambda}z} \mathbf{1}^T \Delta l_z$ as illustrated in Figure 1. The refined condition embeddings aim to provide a more physically plausible representation of light behavior in free space.

As the influence of simulation parameters such as higher relative permittivity increases, resonance effects become more pronounced and weaken the assumption that condition embeddings closely match the ground-truth fields. However, we found that the proposed method remains effective even under these conditions. For a detailed experiment and analysis, refer to Appendix Section E.

4. Experiments

4.1. Experiment Setup

4.1.1. SIMULATION SETUP

In our study, we utilize an open-source FDFD simulation tool Ceviche (Hughes et al., 2019) to generate electromagnetic field data for photonic structures. Specifically, we analyze the field of a metalens structure, simulating only half of the cylindrical symmetry lens to reduce computation time. We implement the FDFD simulation with a grid-based approach at a spatial resolution of 40 points per μm . The simulation domain measures $5.2 \mu m \times 6.85 \mu m$, excluding a $1\text{-}\mu m$ thick perfectly matched layer (PML) at the boundaries. We use SiO_2 (refractive index of approximately 1.46), a material commonly employed in the design of metalenses (Park et al., 2019). This refractive index value is chosen to represent the broadband medium over the entire simulated wavelength range. As demonstrated in Figure 2 (left), we randomly place either SiO_2 or air within the minimum design grid size, a width of 75nm , in the design area. This simulation setup generates data for the E and H fields when visible light passes through the structure.

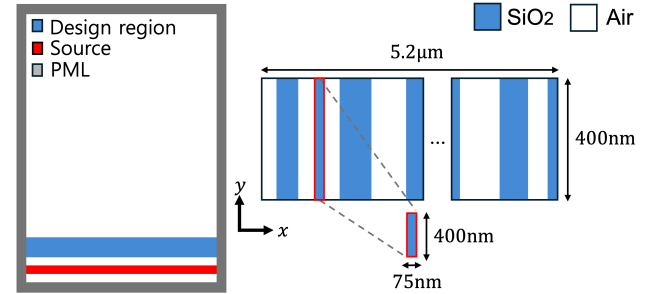


Figure 2: FDFD simulation setup overview. (left) The entire simulation space includes the metalens structure. The blue region represents the design region of the lens, the red line represents the visible light source (TE source), and the gray region represents the PML used to minimize reflections. (right) The design region of the metalens is shown as the blue area in (left).

4.1.2. DATASETS

We aim to predict the E-field for all wavelengths from discrete data in the 400-700nm (visible light) range. To achieve this, we generate field data for discrete wavelengths as our dataset. For each data, different lens structures are randomly placed in the design region, and the field data resulting from FDFD simulations, along with the permittivity(ϵ) of the materials, wavelength(λ), and structural information, are used as pairs for training. The training set consists of 12,000 data sampled randomly at 20nm intervals within the 400-700nm wavelength range. As mentioned above, our goal is to achieve seamless field prediction across the

broadband wavelength. Therefore, to use unseen data for testing, we use 6,020 data each for the test and validation sets, composed of 20 data for each wavelength, sampled at 1nm intervals between 400 and 700nm.

4.1.3. TRAINING OBJECTIVE AND EVALUATION METRIC

Fields typically exhibit different statistics despite the fixed source power. We employ the normalized mean squared error (N-MSE) objective, $L(\mathcal{G}_\theta(a), \mathcal{G}^\dagger(a)) = (\|\mathcal{G}_\theta(a) - \mathcal{G}^\dagger(a)\|_2^2 / \|\mathcal{G}^\dagger(a)\|_2^2)$, to distribute the optimization effort evenly across several field data.

4.2. Results

In the following, we compare the field prediction performance for unobserved wavelengths of Unet (Ho et al., 2020; Gupta & Brandstetter, 2022), FNO (Li et al., 2020), and F-FNO (Tran et al., 2021), commonly used in a surrogate solver study. Moreover, we evaluate our model against NeurOLight (Gu et al., 2022), the state-of-the-art model for field prediction of a narrow wavelength range in EM simulation. To ensure a fair comparison, we configure the hyperparameters of all models to achieve their optimal performance under the specified simulation settings. Detailed information on model architectures is in the Appendix Section C. In EM simulation, while predicting the entire E-field is important, accurately predicting the E-field within the design region is even more crucial. For studies involving surrogate solvers to predict E-fields and subsequently optimize designs, error-free predictions in the design region are essential for designing high-performance photonic devices. However, existing models struggle with the strong resonance effect observed in design regions. These resonances vary with different source wavelengths, even for the same structure, leading to significant errors.

Resonance patterns can arise in the metalens used in our experiments, which is composed of the subwavelength scale structures. As shown in Figure 3 (top), all models except our model exhibit significant errors in the design region. Therefore, our model accurately predicts resonance patterns at intermediate wavelengths within the design region, demonstrating its superior generalization capability. Furthermore, the result indicates that our method improves the overall error compared to the SOTA and significantly reduces the error in the design region.

Our results for unseen wavelengths during training achieved SOTA performance in both test loss across the entire region and loss in the design region, compared to existing models as shown in Figure 3 and Table 1. Specifically, in the design region, our model showed an impressive 80.5% improvement over the previous SOTA model, NeurOLight, for unseen wavelengths and an improvement of 13.2% for seen

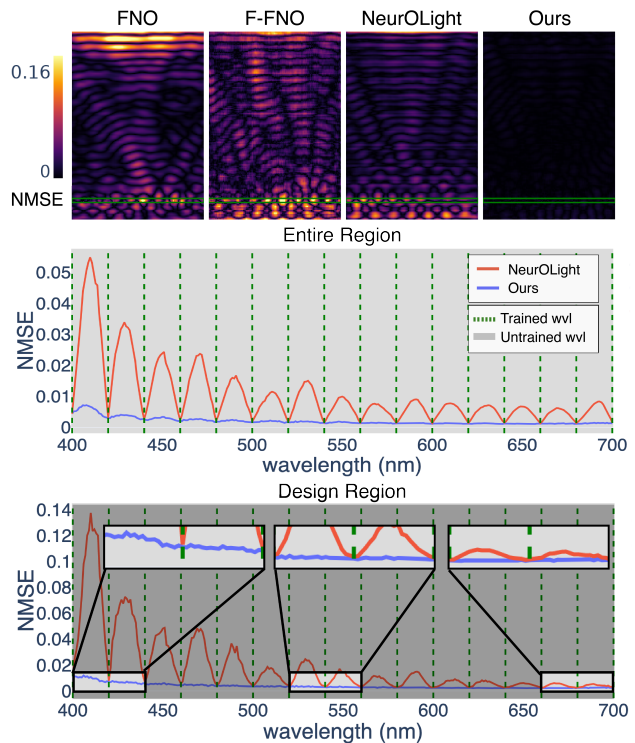


Figure 3: Field interpolation comparisons. (top) Comparison of model errors at 410nm, the unobserved wavelength with the highest error. (middle) Comparison of entire simulation region errors in the 400-700nm wavelength range. (bottom) Comparison of design region errors in the 400-700nm wavelength range.

wavelengths. Moreover, we drastically reduce the number of parameters, achieving a SOTA model with only 0.426 million parameters, a reduction of 74.18% compared to NeurOLight and a reduction of 96.33% compared to Unet. Hence, our model demonstrates performance on par with the existing SOTA models for trained wavelengths while achieving the highest level of performance for untrained wavelengths and model parameter reduction in the current research.

4.3. Ablation Study

4.3.1. CONDITIONING METHODS

We conduct a comparative analysis of our proposed method alongside two other conditioning methods to evaluate the effectiveness of our conditioning method.

Table 2 shows the results of the ablation study on different conditioning methods applied to our model. The conditioning methods considered for comparison include spectral parameter conditioning (Gupta & Brandstetter, 2022; Mao et al., 2024) and the concatenating wave prior (Gu et al., 2022). A detailed explanation on the conditioning meth-

Table 1: Comparisons of field prediction and interpolation. Untrained represents the loss when predicting fields using unobserved wavelength data.

Model	Param (M)	Test loss		Design region test loss	
		Untrained	Trained	Untrained	Trained
Unet	11.60	0.0033	0.0017	0.0062	0.0038
FNO	3.29	0.0133	0.0077	0.0283	0.0251
F-FNO	1.89	0.0331	0.0220	0.0430	0.0371
NeurOLight	1.65	0.0107	0.0020	0.0195	0.0045
Ours	0.43	0.0020	0.0018	0.0038	0.0039

Table 2: Ablation study of several conditioning methods.

Conditioning method	Param (M)	Test loss	
		Untrained	Trained
Spectral parameter conditioning	1.09	0.1376	0.0026
Concatenating wave prior	0.33	0.0028	0.0020
WIME	0.43	0.0020	0.0018

ods is in the Appendix Section D. Although the spectral parameter conditioning method effectively predicts fields of wavelengths observed during training, it fails to generalize across a broadband spectrum, as it does not capture the continuous variation of wave patterns. In contrast, WIME significantly outperforms the concatenating wave prior conditioning method in both trained and untrained wavelength cases. This result demonstrates that our method effectively incorporates condition embeddings that closely align with the spatial and structural features of the fields, leading to more accurate and robust predictions across a continuous range of wavelengths.

Furthermore, we conducted an additional comparative analysis between WIME and other conditioning methods using various models. ‘‘FNO’’ and ‘‘F-FNO’’ refer to methods that incorporate the wave prior by concatenating it with the input data. A detailed description of these conditioning methods is provided in the Appendix Section D.

As shown in Table 3, integrating WIME with FNO enhances prediction performance for unseen wavelengths during training. In particular, applying WIME to F-FNO leads to substantial improvements in field prediction for both trained and untrained wavelengths. The improvement stems from WIME’s ability to effectively incorporate condition information that resembles the ground truth, thereby enhancing the performance of F-FNO. Moreover, WIME successfully addresses the information loss caused by the factorization of the Fourier transform over the problem dimensions. These findings confirm that our conditioning method significantly enhances generalization capability, particularly in scenarios where the model is trained on a limited and discrete set of observed wavelengths.

Table 3: Comparisons of field prediction and interpolation with various conditioning methods and models.

Model	Param (M)	Test loss		Design region test loss	
		Untrained	Trained	Untrained	Trained
FNO	3.29	0.0133	0.0077	0.0283	0.0251
FNO-WIME	3.30	0.0100	0.0084	0.0277	0.0288
F-FNO	1.89	0.0331	0.0220	0.0430	0.0371
F-FNO-WIME	1.92	0.0076	0.0067	0.0147	0.0147

 Table 4: Ablation study for ϵ_r term in wave prior.

ϵ_r term	Test loss	
	Untrained	Trained
✓	0.0024	0.0021
	0.0020	0.0018

4.3.2. PERMITTIVITY IN THE WAVE PRIOR

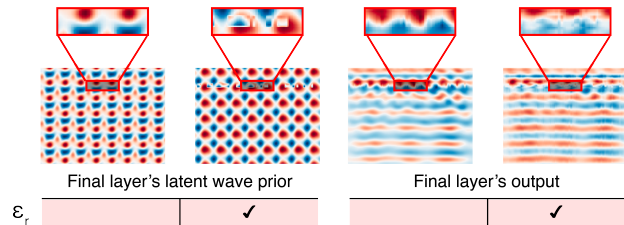


Figure 4: Visualization of the features of condition information and outputs from the final layers of our model for a specific part of the entire region for 400nm wavelength data. (left) The latent wave prior in the final layer, excluding and including the ϵ_r term. (right) The output of the final layer without and with considering the ϵ_r term. The magnified sections are part of the region where structures exist.

As shown in Table 4, we demonstrate performance improvements resulting from the exclusion of the ϵ_r term in the wave prior through an ablation study. To understand the underlying reason for this improvement, we analyze both the latent wave prior and the output of the last layer in our model. Figure 4 (left) shows the latent wave prior before element-wise multiplication in the last layer of our model. Sharp artifacts emerge in regions containing structures, when the wave prior includes the ϵ_r term. This occurs because WIME utilizes shallow 1×1 convolutional layers, which preserve discretization invariance and maintain the spatial structure of the refined wave prior. Figure 4 (right) presents the final layer outputs of our model. The result reveals that when the ϵ_r term is included in the wave prior, physically implausible artifacts appear throughout the entire region. Based on these findings, we conclude that incorporating the ϵ_r term in the wave prior introduces unintended bias, negatively impact-

ing the model’s field prediction accuracy and generalization capabilities.

4.3.3. HYPERPARAMETERS OF FGCS OPERATOR

We assess the validity of the hyperparameters (groups and channels) and design choices (weight sharing and channel shuffling) of the proposed FGCS operator by conducting an extensive ablation study, as shown in Table 5. We increase the number of groups in proportion to the growth of channels to consider a consistent number of parameters in all cases. Row 9 presents the FGCS operator used in our model. Rows 1-3, which do not utilize weight sharing and channel shuffling in the Fourier domain, follow the same operational form as described in a previous study (Kim et al., 2024). When only weight sharing is employed (rows 4-5), the prediction of fields for both unobserved and observed wavelengths during the training demonstrates worse performance compared to that in the previous study (Kim et al., 2024) due to a substantially small number of parameters. However, as the number of groups and channels increases, the performance becomes competitive. Notably, the performance in predicting the fields for unobserved wavelengths during training is better. Thus, the weight-sharing scheme significantly aids in generalization for the unobserved spectral parameters.

In addition, comparing the previous method (Kim et al., 2024) (rows 2-3) with the case where only channel shuffling is used (rows 6-7), the field prediction performances for both untrained and trained wavelengths are better. This suggests that employing the channel shuffling method with the grouping method significantly improves the overall performance. Following the design configuration of the FGCS operator (rows 8-9), we can construct a parameter-efficient model that achieves an overall performance improvement as the number of groups and channels is heightened. Although the FGCS operator shows slightly lower prediction performance for trained wavelengths than when only a channel shuffling scheme is employed, it demonstrates superior performance for untrained wavelengths. Therefore, the proposed FGCS operator contributes to improving the prediction performance for unseen broadband spectrums during training. Rows 10-13 present varying performances when increasing the model width. The performance improvement of the FGCS operator becomes increasingly significant with the addition of more channels. In particular, there is a substantial improvement when the number of groups and channels increases to 8 and 128, respectively. We believe that excessively sparse constructions of weight tensors and information compensating with channel shuffling may improve the generalization capacity of large models.

Table 5: Ablation of design components of proposed FGCS operator. The ✓ indicates the use of the design components.

Weight sharing	Channel shuffling	Groups	Channels	Param (M)	Test loss	
					Untrained	Trained
		1	32	0.42	0.0041	0.0036
		2	48	0.56	0.0028	0.0019
		4	64	0.65	0.0025	0.0017
✓		2	48	0.37	0.0040	0.0034
✓		4	64	0.40	0.0023	0.0020
	✓	2	48	0.58	0.0033	0.0028
	✓	4	64	0.68	0.0021	0.0015
✓	✓	2	48	0.39	0.0037	0.0030
✓	✓	4	64	0.43	0.0020	0.0018
		8	128	1.90	0.0016	0.0009
✓		8	128	1.31	0.0012	0.0009
	✓	8	128	2.00	0.0015	0.0008
✓	✓	8	128	1.41	0.0011	0.0008

5. Conclusion

In this study, we introduce Wave-Informed element-wise Multiplicative Encoding (WIME) and Fourier Group Convolution Shuffling (FGCS) to overcome the limitations of existing FNO-based surrogate solvers in predicting electric fields across a continuous and broad spectrum of wavelengths while significantly reducing parameter complexity. Our experimental results demonstrate that the proposed model achieves state-of-the-art accuracy in predicting field distributions within both the design region and the field propagation region, outperforming existing models. Specifically, our model achieves an 80.5% improvement over NeurOLight in predicting field profiles at unobserved wavelengths and a 13.2% enhancement for trained (observed) wavelengths. Additionally, it reduces the number of parameters by 74.18% compared to NeurOLight and by 96.33% compared to U-Net. Furthermore, our model accurately captures nonlinearity of resonance patterns in subwavelength photonic structures, demonstrating its ability to handle complex electromagnetic phenomena.

These results suggest that our approach has the potential to replace conventional numerical methods for solving PDEs, offering a powerful solution for unseen simulation environments and significantly enhancing computational efficiency in electromagnetic simulations. Moving forward, we will conduct a theoretical investigation to clarify the universal approximation properties of our neural operator-based framework, further strengthening its theoretical foundations and applicability.

References

- Azizzadenesheli, K., Kovachki, N., Li, Z., Liu-Schiaffini, M., Kossaifi, J., and Anandkumar, A. Neural operators for accelerating scientific simulations and design. *Nature Reviews Physics*, pp. 1–9, 2024.
- Bae, M., Kim, C., Lee, S., Choi, M., Lee, M., Jung, H., Kwon, H., and Chung, H. Topology optimization of lithium niobate mode converter. In *Conference on Lasers and Electro-Optics/Pacific Rim*, pp. We2A.2. Optica Publishing Group, 2024.
- Brunton, S. L., Noack, B. R., and Koumoutsakos, P. Machine learning for fluid mechanics. *Annual review of fluid mechanics*, 52(1):477–508, 2020.
- Cao, S. Choose a transformer: Fourier or galerkin. *Advances in neural information processing systems*, 34: 24924–24940, 2021.
- Chung, H. and Miller, O. D. High-na achromatic metalenses by inverse design. *Optics Express*, 28(5):6945–6965, 2020.
- Dorodnyy, A., Smajic, J., and Leuthold, J. Mie scattering for photonic devices. *Laser & Photonics Reviews*, 17(9): 2300055, 2023.
- Gold, H., Pajovic, S., Mukherjee, A., and Boriskina, S. V. Gaga for nonreciprocal emitters: genetic algorithm gradient ascent optimization of compact magnetophotonic crystals. *Nanophotonics*, 13(5):773–792, 2024.
- Gu, J., Gao, Z., Feng, C., Zhu, H., Chen, R., Boning, D., and Pan, D. Neurolight: A physics-agnostic neural operator enabling parametric photonic device simulation. *Advances in Neural Information Processing Systems*, 35: 14623–14636, 2022.
- Guibas, J., Mardani, M., Li, Z., Tao, A., Anandkumar, A., and Catanzaro, B. Adaptive fourier neural operators: Efficient token mixers for transformers. *arXiv preprint arXiv:2111.13587*, 2021.
- Gupta, J. K. and Brandstetter, J. Towards multi-spatiotemporal-scale generalized pde modeling. *arXiv preprint arXiv:2209.15616*, 2022.
- Hao, Z., Wang, Z., Su, H., Ying, C., Dong, Y., Liu, S., Cheng, Z., Song, J., and Zhu, J. Gnot: A general neural operator transformer for operator learning. In *International Conference on Machine Learning*, pp. 12556–12569. PMLR, 2023.
- Ho, J., Jain, A., and Abbeel, P. Denoising diffusion probabilistic models. *Advances in neural information processing systems*, 33:6840–6851, 2020.
- Hughes, T. W., Minkov, M., Williamson, I. A., and Fan, S. Adjoint method and inverse design for nonlinear nanophotonic devices. *ACS Photonics*, 5(12):4781–4787, 2018.
- Hughes, T. W., Williamson, I. A., Minkov, M., and Fan, S. Forward-mode differentiation of maxwell’s equations. *ACS Photonics*, 6(11):3010–3016, 2019.
- Kang, C., Park, C., Lee, M., Kang, J., Jang, M. S., and Chung, H. Large-scale photonic inverse design: computational challenges and breakthroughs. *Nanophotonics*, 2024a. doi: doi:10.1515/nanoph-2024-0127.
- Kang, C., Seo, J., Jang, I., and Chung, H. Adjoint method-based fourier neural operator surrogate solver for wavefront shaping in tunable metasurfaces. *iScience*, 2024b.
- Kim, M., Park, J., and Shin, J. Efficient fourier neural operators by group convolution and channel shuffling. In *ICLR 2024 Workshop on AI4DifferentialEquations In Science*, 2024. URL <https://openreview.net/forum?id=TyglzCofE3>.
- Kovachki, N., Li, Z., Liu, B., Azizzadenesheli, K., Bhattacharya, K., Stuart, A., and Anandkumar, A. Neural operator: Learning maps between function spaces with applications to pdes. *Journal of Machine Learning Research*, 24(89):1–97, 2023.
- Kuznetsov, A. I., Brongersma, M. L., Yao, J., Chen, M. K., Levy, U., Tsai, D. P., Zheludev, N. I., Faraon, A., Arbabi, A., Yu, N., et al. Roadmap for optical metasurfaces. *ACS photonics*, 11(3):816–865, 2024.
- Lee, S., Hong, J., Kang, J., Park, J., Lim, J., Lee, T., Jang, M. S., and Chung, H. Inverse design of color routers in cmos image sensors: toward minimizing interpixel crosstalk. *Nanophotonics*, 13(20):3895–3914, 2024.
- Li, Z., Kovachki, N., Azizzadenesheli, K., Liu, B., Bhattacharya, K., Stuart, A., and Anandkumar, A. Fourier neural operator for parametric partial differential equations. *arXiv preprint arXiv:2010.08895*, 2020.
- Li, Z., Meidani, K., and Farimani, A. B. Transformer for partial differential equations’ operator learning. *arXiv preprint arXiv:2205.13671*, 2022a.
- Li, Z., Peng, W., Yuan, Z., and Wang, J. Fourier neural operator approach to large eddy simulation of three-dimensional turbulence. *Theoretical and Applied Mechanics Letters*, 12(6):100389, 2022b.
- Li, Z., Pestourie, R., Park, J.-S., Huang, Y.-W., Johnson, S. G., and Capasso, F. Inverse design enables large-scale high-performance meta-optics reshaping virtual reality. *Nature communications*, 13(1):1–11, 2022c.

- Li, Z., Huang, D. Z., Liu, B., and Anandkumar, A. Fourier neural operator with learned deformations for pdes on general geometries. *Journal of Machine Learning Research*, 24(388):1–26, 2023.
- Li, Z., Kovachki, N., Choy, C., Li, B., Kossaifi, J., Otta, S., Nabian, M. A., Stadler, M., Hundt, C., Azizzadenesheli, K., et al. Geometry-informed neural operator for large-scale 3d pdes. *Advances in Neural Information Processing Systems*, 36, 2024a.
- Li, Z., Shu, D., and Barati Farimani, A. Scalable transformer for pde surrogate modeling. *Advances in Neural Information Processing Systems*, 36, 2024b.
- Mao, C., Lupoiu, R., Dai, T., Chen, M., and Fan, J. A. Towards general neural surrogate solvers with specialized neural accelerators. *arXiv preprint arXiv:2405.02351*, 2024.
- Nieto-Vesperinas, M. Fundamentals of mie scattering. In *Dielectric Metamaterials*, pp. 39–72. Elsevier, 2020.
- Park, J.-S., Zhang, S., She, A., Chen, W. T., Lin, P., Yousef, K. M., Cheng, J.-X., and Capasso, F. All-glass, large metalens at visible wavelength using deep-ultraviolet projection lithography. *Nano letters*, 19(12):8673–8682, 2019.
- Pathak, J., Subramanian, S., Harrington, P., Raja, S., Chattopadhyay, A., Mardani, M., Kurth, T., Hall, D., Li, Z., Azizzadenesheli, K., et al. Fourcastnet: A global data-driven high-resolution weather model using adaptive fourier neural operators. *arXiv preprint arXiv:2202.11214*, 2022.
- Rahman, M. A., Ross, Z. E., and Azizzadenesheli, K. U-no: U-shaped neural operators. *arXiv preprint arXiv:2204.11127*, 2022.
- Raonic, B., Molinaro, R., Rohner, T., Mishra, S., and de Bezenac, E. Convolutional neural operators. In *ICLR 2023 Workshop on Physics for Machine Learning*, 2023.
- Seo, J., Jo, J., Kim, J., Kang, J., Kang, C., Moon, S., Lee, E., Hong, J., Rho, J., and Chung, H. Deep-learning-driven end-to-end metalens imaging. *arXiv preprint arXiv:2312.02669*, 2023.
- Setareh, M., De Gille, R., Cadusch, J., Wen, D., Kim, S., and Crozier, K. B. High efficiency triple-helix solenoid beam generated by dielectric metasurface. *ACS Photonics*, 11(9):3486–3491, 2024.
- Tran, A., Mathews, A., Xie, L., and Ong, C. S. Factorized fourier neural operators. *arXiv preprint arXiv:2111.13802*, 2021.
- Vaswani, A., Shazeer, N., Parmar, N., Uszkoreit, J., Jones, L., Gomez, A. N., Kaiser, Ł., and Polosukhin, I. Attention is all you need. *Advances in neural information processing systems*, 30, 2017.
- Wang, J., Sciarrino, F., Laing, A., and Thompson, M. G. Integrated photonic quantum technologies. *Nature Photonics*, 14(5):273–284, 2020.
- Xie, E., Wang, W., Yu, Z., Anandkumar, A., Alvarez, J. M., and Luo, P. Segformer: Simple and efficient design for semantic segmentation with transformers. *Advances in neural information processing systems*, 34:12077–12090, 2021.
- Xie, S., Girshick, R., Dollár, P., Tu, Z., and He, K. Aggregated residual transformations for deep neural networks. In *Proceedings of the IEEE conference on computer vision and pattern recognition*, pp. 1492–1500, 2017.
- Xue, W., Zhang, H., Gopal, A., Rokhlin, V., and Miller, O. D. Fullwave design of cm-scale cylindrical metasurfaces via fast direct solvers. *arXiv preprint arXiv:2308.08569*, 2023.
- Yoon, H., Lee, H. H., Ahn, Y. N., Choi, E.-H., Lee, J., and Kim, H. Mechanism of nanovoid formation at the zno-glass interface in planar multilayered structures of alox-zno-glass. *Journal of the American Ceramic Society*, 99(8):2809–2815, 2016.
- Zhou, D. and Huang, D. A review on the progress, challenges and prospects in the modeling, simulation, control and diagnosis of thermodynamic systems. *Advanced Engineering Informatics*, 60:102435, 2024.

A. Nonlinearity of Subwavelength Photonic Structure Resonance

Mie scattering (Dorodnyy et al., 2023; Nieto-Vesperinas, 2020), a fundamental mechanism describing the interaction of electromagnetic waves with particles smaller than the wavelength of light, is pivotal in understanding resonance phenomena in subwavelength photonic structures. The mathematical formulation of Mie scattering is expressed through an infinite series of spherical harmonics, where each term represents a different mode of scattering:

$$\sigma(\lambda, r) = \frac{2\pi}{k^2} \sum_{n=1}^{\infty} (2n+1) (|a_n|^2 + |b_n|^2)$$

where λ is the wavelength, r is the radius of the particle, $k = \frac{2\pi}{\lambda}$ is the wave number, and a_n, b_n are the scattering coefficients for electric and magnetic modes, respectively. The nonlinearity arises from the complex interaction between these modes, which can be highly sensitive to structural and material parameters, making accurate predictions difficult. Furthermore, high Q-factors are indicative of sharp resonance peaks and narrow bandwidths in the response of photonic structures, which implies that the system has a high selectivity in frequency response. While beneficial for many applications, high Q-factors also mean that the resonance is extremely sensitive to slight deviations in system parameters, such as changes in material properties or geometric alterations. This sensitivity leads to significant challenges in predicting the behavior of the system under slightly altered conditions:

$$Q = \frac{\omega_0}{\Delta\omega}$$

where ω_0 is the resonance frequency and $\Delta\omega$ is the bandwidth of the resonance.

At subwavelength scales, interactions between light and matter involve complex phenomena like electric and magnetic Mie resonances. Therefore, surrogate solvers trained at a single wavelength struggle to predict nonlinear resonances in regions with matter across broadband wavelengths. In this work, the proposed model overcomes this challenge, accurately predicting resonances arising from structures.

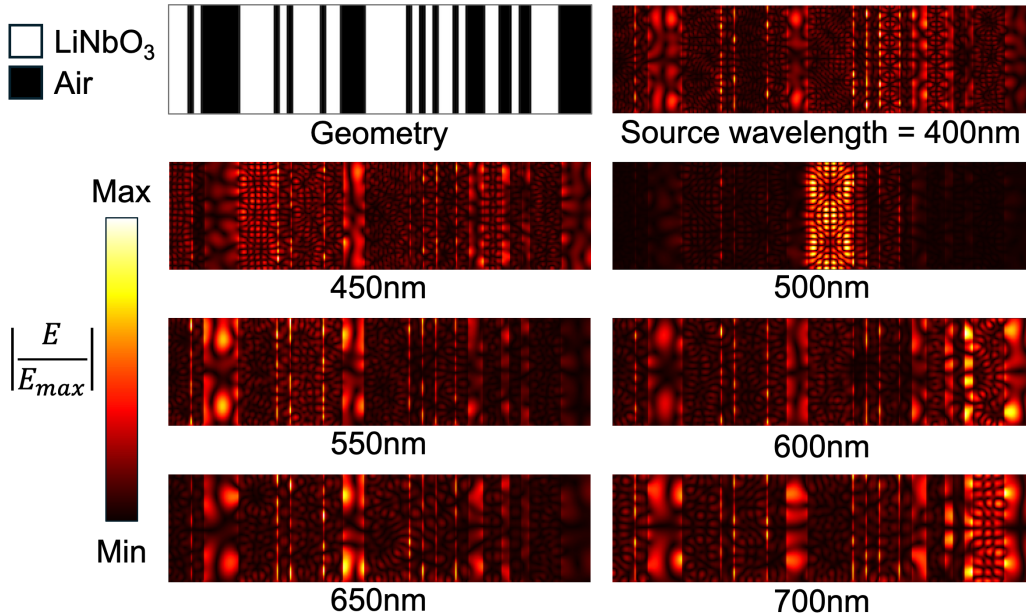


Figure 5: Using the FDTD simulation, the E-field at the same time step is visualized for a design region composed of LiNbO₃ and Air. This visualization confirms that resonance occurs nonlinearly with respect to wavelength.

B. Training Details

Our model training runs for 200 epochs with 32 batch size. The best model is selected based on the lowest loss in predicting previously unseen wavelengths during the training phase. We employ the GELU (Gaussian Error Linear Unit) activation

function and the AdamW optimizer with the following parameters: a learning rate of 0.002, beta values of (0.9, 0.999), epsilon set to 10^{-8} , and a weight decay factor of 0.0001. To dynamically adjust the learning rate, we utilize a cosine annealing learning rate scheduler with a minimum learning rate of 0.00001. Mode is set to (50, 60). We leverage PyTorch, and the training process is conducted using a single RTX 6000 Ada.

C. Detailed Model Architectures

C.1. Unet

We use a 4-level modern convolutional Unet architecture with an initial channel size of 16. Each level consists of two residual blocks with GELU activation function and Group Normalization. We concatenate the refined wave prior with the input for the conditioning method.

C.2. FNO

We set the number of Fourier layers and the number of channels in each Fourier layer to 5 and 32, respectively. The frequency modes for the z and x axes are set to [32, 10]. In addition, the lifting operator is a linear operator, and the projection operator is a 2-layer feed-forward network with GELU activation and a dimension of 128. We concatenate the refined wave prior with the input to inject condition information.

C.3. F-FNO

We employ 12 Fourier layers, each consisting of 64 channels. The frequency modes for the z and x axes are set to [50, 60]. The lifting operator is a linear operator, and the final projection operator is a 2-layer feed-forward network with GELU activation function and a dimension of 256. To incorporate condition information, we concatenate the refined wave prior with the input.

C.4. NeurOLight

We use 12 Fourier layers with 64 channels each. The frequency modes for the z and x axes are set to [50, 60]. The channel expansion factor for the convolutional modules in the NeurOLight layers is configured to be 2. To inject condition information, we concatenate the wave prior with the input. During training, we implement stochastic network depth with a rate of 0.1 to the residual NeurOLight layers to alleviate overfitting.

C.5. Ours

We use 12 layers with 64 channels each and specify the number of groups as 4. The frequency modes for the z and x axes are configured as [50, 60]. We implement a channel expansion scheme with a factor of 2 for the 2-layer feed-forward network in the layers, inspired by (Xie et al., 2021; Gu et al., 2022). The lifting operator is linear, and the final projection operator is a 2-layer feed-forward network with GELU activation and a dimension of 256.

D. Detailed Conditioning Methods

D.1. Spectral parameter conditioning

The spectral parameter conditioning method transforms the scalar wavelength into a vector via sinusoidal embedding (Vaswani et al., 2017). It then employs a two-layer feed-forward network to project the embeddings onto a higher-dimensional space of $4 \times$ hidden channels. The embeddings are mapped to the Fourier space using the module named FreqLinear module described in (Gupta & Brandstetter, 2022). Finally, the embeddings in the Fourier space are mode-wise multiplied with the input of the Fourier integral kernel to perform parameter conditioning in the spectral domain.

D.2. Concatenating wave prior

The concatenating wave prior injects the condition information by simply concatenating the given refined wave prior to the input data.

E. Additional Experiments for the Weakened Precluded Assumption

We conducted additional experiments to evaluate the performance of our proposed method when the precluded assumption (that the field and condition data have high similarity) becomes weak. We set up the simulation with a more complex field using a material with higher relative permittivity (lithium niobate, refractive index $n \approx 2.3$)¹.

Table 6: Comparisons of field prediction and interpolation with high relative permittivity.

Model	Param (M)	Test loss		Design region test loss	
		Untrained	Trained	Untrained	Trained
Unet	11.60	0.0172	0.0178	0.0275	0.0287
FNO	3.29	0.1207	0.1204	0.3336	0.3338
FNO-WIME	3.30	0.1202	0.1229	0.3513	0.3487
F-FNO	1.89	0.1006	0.1062	0.1930	0.1921
F-FNO-WIME	1.92	0.0679	0.0679	0.1409	0.1406
NeurOLight	1.65	0.0171	0.0116	0.0339	0.0267
Ours	0.43	0.0079	0.0081	0.0185	0.0179

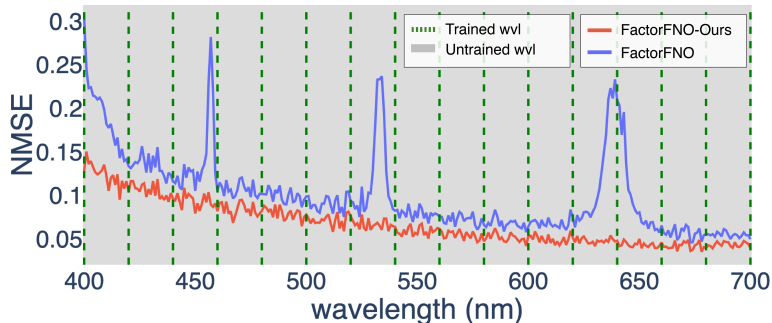


Figure 6: Field interpolation comparisons of F-FNO with simply concatenating conditioning and our conditioning method. Comparison of entire simulation region errors in the 400-700nm wavelength range.

FNO is inefficient in terms of the number of parameters. Despite having fewer layers and widths and lacking additional modules like fully connected layers, it has the highest number of parameters among the neural operators compared. As shown in Table 6², FNO struggles to learn complex optical properties even when our conditioning method is applied due to the limited learning capacity caused by the given problems. In contrast, F-FNO has sufficient capacity because of its superior parameter efficiency, which allows for many layers, widths, and additional MLPs. F-FNO demonstrates inferior performance despite its superior learning capacity if concatenating the wave prior with input data for conditioning. In particular, it exhibited peaks in the loss at specific wavelengths (Figure 6). On the other hand, applying our conditioning method to F-FNO significantly improves the field prediction performance and resolves the peak problem. This demonstrates that our method effectively helps to learn complex optical phenomena for a wide range of wavelengths when sufficient learning capacity is available. While NeurOLight exhibits superior performance in field inference, it struggles to predict E-field across the broadband spectrum. However, our method still demonstrates the best performance even when the precluded assumption becomes weak.

F. Weakening the Precluded Assumption

The proposed model element-wisely multiplies latent condition data at every layer. Although the conditioning method serves as a powerful regularization means for interpolation on a wide range of conditions, it can have adverse effects when the

¹Permittivity is the square of the refractive index, denoted by n , which indicates how much light is refracted when it passes through a medium. Therefore, materials with higher permittivity have higher refractive indices. Consequently, when light passes through a material with high permittivity, it slows down more than in a material with lower permittivity, resulting in a more complex field pattern.

²The inference performance for untrained wavelengths often appears better than for trained wavelengths. This is because nonlinear optics phenomena (diffraction, resonance) caused by the high epsilon occur strongly, resulting in the loss exhibiting a slightly exponential change with respect to the wavelength. Consequently, if spectrum (condition) interpolation is successful, it can result in lower loss values for untrained wavelengths.

Table 7: Field prediction and interpolation comparisons between injecting the condition into all but the last l layers when relative permittivity is high.

Model	Param (M)	Test loss		Design region test loss	
		Untrained	Trained	Untrained	Trained
Ours	0.43	0.0079	0.0081	0.0185	0.0179
Ours ($l=1$)	0.42	0.0076	0.0077	0.0177	0.0178
Ours ($l=2$)	0.41	0.0075	0.0076	0.0175	0.0176
Ours ($l=3$)	0.40	0.0082	0.0084	0.0191	0.0195

precluded assumption is weakened due to more complex fields simulated from materials with high relative permittivity.

To assess the effects of weakening the assumption underlying this work, we conduct an ablation study, injecting information into layers except for the last l layers.

As shown in Table 7, injecting the condition into all but the last 1 and 2 layers ($l = 1, 2$) reflects weakened assumption well and leads to performance improvement. However, injecting the condition into all but the final 3 layers ($l = 3$) results in a decrease in both field inference performance and interpolation performance. This demonstrates the trade-off between the powerful regularization of our conditioning method and reflecting the weakened assumption.

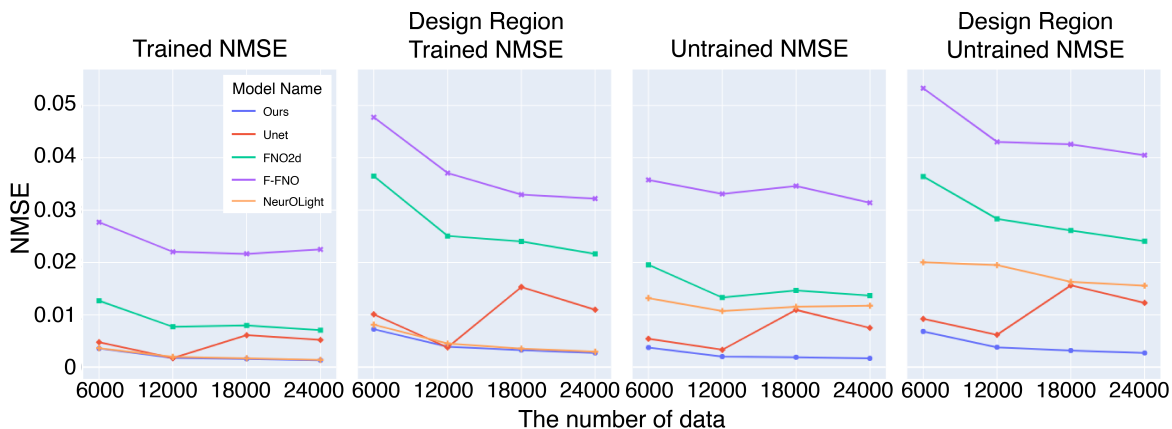


Figure 7: Comparisons of field prediction and interpolation across varying dataset sizes.

G. Additional Experiments for Evaluating Performance across Varying Dataset Sizes

To analyze the dependency between dataset sizes and the performance of our method, we executed an additional experiment to evaluate performance with varying dataset sizes. We used the 400–700 nm wavelength range dataset, randomly sampled at 20 nm intervals, the same as the main experiments. The conditioning method used in the compared models except our method is to concatenate the wave prior with input data (“Concatenating wave prior”) As shown in Fig 7, our method demonstrated better both interpolation performance and field prediction performance of trained wavelengths for the overall dataset’s sizes. The results indicated that the proposed conditioning method effectively injects condition information. Furthermore, the results demonstrate that the proposed conditioning method shows minimal performance variance regarding dataset size across both trained and untrained wavelengths. This implies that the method effectively incorporates sufficient physical information even with limited data and efficiently reflects the varying physical features with continuously changing wavelengths.